Proceedings 10th NUMGE 2023
10th European Conference on Numerical Methods in Geotechnical Engineering
Zdravkovic L, Kontoe S, Taborda DMG, Tsiampousi A (eds)

https://doi.org/10.53243/NUMGE2023-359

A two-dimensional effective stress framework for modelling 'whole-life' soil strength changes

C.D. O'Loughlin[1], Y. Wang[1,2], Z. Zhou[1,2], C. Gaudin[1]

[1] *Centre for Offshore Foundation Systems, Oceans Graduate School, University of Western Australia, Australia*

[2] *Norwegian Geotechnical Institute, Norway*

ABSTRACT: The undrained shear strength of fine-grained soils changes with time, reducing due to pore pressure generation, and increasing during consolidation. This paper describes an effective stress framework, implemented within a two-dimensional computational domain, that relates generation of pore pressure to accumulated plastic shear strain, allowing undrained shear strength to be calculated within the context of critical-state soil mechanics. The magnitude and distribution of plastic shear strain around objects buried in soil is determined through a series of large deformation finite element analyses, and these spatial distributions are described using a strain influence function in the framework to calculate the extent and magnitude of excess pore pressure, and in turn the mobilised soil strength around the buried object. The potential of the framework is examined through a series of example simulations that demonstrate the changing soil strength that would be mobilised by an embedded foundation in response to varying loading histories.

Keywords: offshore; soil strength; effective stress; cyclic loading; consolidation

1 INTRODUCTION

A key input to geotechnical design is selection of the operative soil strength. Soil strength is governed by several factors, including the mode of failure, drainage conditions, strain rates and strain softening. The dependence of soil strength on shearing mode is well-known. For example, the stress paths followed by elements along the failure surface for a shallow foundation can be simulated in triaxial compression, simple shear and triaxial extension tests (Andersen et al. 2008). The highest variation in undrained shear strength, s_u, between these shearing modes is between triaxial compression and extension, where s_u in triaxial compression can be up to twice that in triaxial extension (Krabbenhøft et al. 2019).

In other instances it may be necessary to account for the different strain rates that apply in the measurement of s_u (e.g. in a cone penetrometer test) and in the particular geotechnical design problem of interest. For instance, allowing for strain rate effects becomes important when considering the dynamic penetration of free-fall anchors and penetrometers, where the velocity of the body as it penetrates the soil can be around 20 m/s, with operative strengths that can be over twice that determined from a 'conventional' in situ penetrometer test.

A further consideration is the changes in strength due to strain softening and consolidation. Excess pore pressures develop as shear strains increase, causing a softening effect on soil strength, but with time these pore pressures will dissipate, causing the soil strength to increase or 'harden'.

The range of strength discussed above is demonstrated by Figure 1, which shows that the range of strength for a reconstituted silt as measured by penetrometer tests (Chow et al. 2020) can vary by a factor of 20. Temporal changes in soil strength are well recognised in some areas of offshore geotechnical design. For instance, installation of piles (either by driving or with the assistance of suction) causes remoulding of the soil at the pile wall. The frictional component of axial pile capacity is well recognised to increase with time after installation, and this 'setup' effect is typically allowed for in design. Other examples where consolidation-induced improvements in seabed strength are often allowed for in offshore design include bearing capacity increases underneath shallow foundations and drag anchor capacity increases between installation and hook-up.

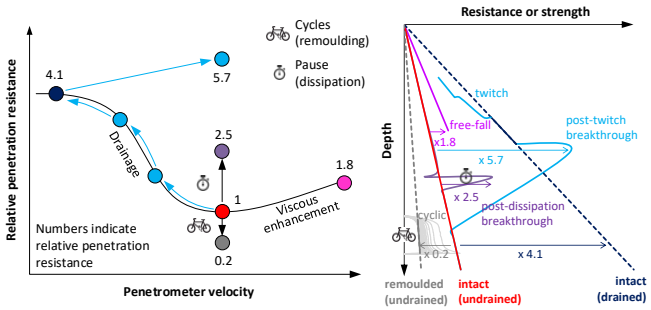

Figure 1. The range of penetration resistance measured in a reconstituted carbonate silt (after Chow et al. 2020)

Calculation approaches that allow for the change in soil strength range in complexity. For instance, the typical design approach to account for setup effects in piles is to adjust the intact value of s_u to a remoulded value via the soil sensitivity and to allow for time-dependent consolidation-induced soil strength increases soils using closed-form consolidation solutions (Randolph 2013). Accounting for soil strength changes due to consolidation beneath shallow foundations can be achieved by applying the undrained shear strength ratio, s_u/σ'_v for the soil to the spatially varying changes in vertical effective stress, σ'_v, beneath the foundation. More sophisticated calculation approaches have been proposed, including coupled finite element analyses (e.g., Gourvenec et al. 2014; Feng and Gourvenec 2015) and critical-state inspired calculation frameworks (Cocjin et al. 2017; Zhou et al. 2019). The latter approach is attractive as it can deal with complex time histories of cyclic loading in a very time efficient manner, making it more suited for use in design practice than coupled finite element analyses. To date, critical state calculation frameworks that couple excess pore pressure generation and dissipation have only been implemented for a one-dimensional computational domain, limiting their application to boundary value problems that can be idealised as one-dimensional.

This paper addresses this limitation by summarising recent work that has extended the one-dimensional effective stress framework proposed by Zhou et al. (2019) to allow for applications in a two-dimensional computational domain. The merit of the new framework is explored via simulations of the capacity mobilisation response of an embedded plate anchor.

2 2D EFFECTIVE STRESS FRAMEWORK

2.1 Overview

The 2D effective stress framework extends the original framework proposed by Zhou et al. (2019) that allows the evolution and spatial distribution of soil strength to be calculated in response to the generation and dissipation of excess pore pressure. Figure 2 shows the nomenclature and sign convention adopted here. $\hat{x}$ and $\hat{z}$ are normalised (by the object diameter, D) distances used to establish the 2D coordinate system, such that generalised object movements can be made by prescribing displacement increments in any direction through a combination of $d\hat{x}$ (horizontal increments) and $d\hat{z}$ (vertical increments). $\hat{x}_c$ and $\hat{z}_c$ denote the current coordinates of the object centroid.

The components and analysis procedure of the framework are presented in Figure 2. A 2D strain influence zone is defined that delimitates the region of soil around the object within which shear strains accumulate. A strain influence function, $\mu(\hat{x},\hat{z})$, is then defined to calculate the incremental shear strain, $d\xi(\hat{x},\hat{z})$, in the vicinity of the object due to the incremental displacement, $d\hat{\delta}$ (e.g. movement along the vertical direction as shown in Figure 2b). Integration of incremental shear strain over the influence zone yields the reference accumulated shear strain, ξ_{ref}. As the object displaces within the soil domain, $\xi(\hat{x}, \hat{z})$ accumulates according to the strain influence function (Figure 2c).

Shearing-induced excess pore pressure, denoted as $u_e(\hat{x}, \hat{z})$, is generated in a rate-dependent form according to the shear strain rate $d\xi(\hat{x}, \hat{z})$, leading to a reduction in vertical effective stress, $\sigma'_v(\hat{x}, \hat{z})$. This is represented by the path A-B in the specific volume-vertical effective stress space (v-σ'_v) on Figure 3. σ'_v moves towards the fully remoulded strength line (denoted RSL) at constant specific volume causing accumulation of excess pore pressure, u_e (Figure 2d). Maintained loads on the object will induce a total stress change and alter the equilibrium vertical effective stress, $\sigma'_{v,eqm}$, and generate additional excess pore pressure (Figure 2e) that is either positive or negative depending on the loading direction and the location of the soil element relative to the object.

During consolidation, excess pore pressure dissipation, $u_e(\hat{x},\hat{z})$, is calculated over the soil domain using a hyperbolic rate-form equation, and this change in excess pore pressure is used to update the current vertical effective stress, $\sigma'_v(\hat{x}, \hat{z})$ (Figure 2f). In v-σ'_v space, this is represented by the fully-consolidated path B-C-D on Figure 3, first along the URL (unload-reload line) and then along the NCL (normal compression line) until the vertical effective stress equilibrates at $\sigma'_{v,eqm}$.

The average undrained shear strength, $s_{u,av}$, mobilised by the object is calculated by a weighted average of local undrained shear strength within the influence zone (Figure 2g). The progressive mobilisation of $s_{u,mob}$ with displacement is considered using a non-linear strength-displacement model (Equation 17), allowing the geotechnical capacity, q, to be calculated as $q = N_c s_{u,mob}$, where N_c is the bearing capacity factor. The various equations associated with the preceding description are referred to in Figure 2 and are listed in Table 1 (Equations 1-15). Developments required to extend the framework from one to two dimensions are summarised in the following sections.

2.2 Strain influence function

Zhou et al. (2019) adopted a macro-element approach, whereby the response is encapsulated by representing the foundation as a 'point' with triangular influence zones defining the extent and magnitude of shear strain and pore pressure development. In the 2D effective stress framework the spatial distribution of accumulated plastic shear strain, ξ, is quantified using a strain influence function that is established using results from large deformation finite element (LDFE) analyses.

Table 1. Components and equations of framework

Modules	Components	Equations	Equation no.
Initial state	In situ geostatic effective stress	$\sigma'_v(\hat{x},\hat{z}) = \gamma'\hat{z}$	(1)
	Initial specific volume	$v_i(\hat{x},\hat{z}) = \Gamma_{NCL} - \lambda \ln[OCR(\hat{x},\hat{z})\sigma'_{v,0}(\hat{x},\hat{z})] + \kappa \ln[OCR(\hat{x},\hat{z})]$	(2)
	Effective stress on NCL	$\sigma'_{v,NCL}(\hat{x},\hat{z}) = \exp\left(-\frac{\Gamma_{NCL} - v(\hat{x},\hat{z})}{\lambda}\right)$	(3)
	Effective stress on RSL	$\sigma'_{v,RSL}(\hat{x},\hat{z}) = \left[\frac{s_u}{\sigma'_v}\right]_{NC} \frac{\sigma'_{v,0}(\hat{x},\hat{z})}{\Phi_{steady} S_t} \exp\left(\frac{\Lambda\left[\Gamma_{NCL} - v_i(\hat{x},\hat{z}) - \lambda \ln[\sigma'_{v,0}(\hat{x},\hat{z})]\right]}{\lambda - \kappa}\right)$	(4)
Undrained loading	Strain influence function	$\mu(\hat{x},\hat{z}) = h \begin{cases} 1, & \lvert\hat{x}\rvert \le \beta_w, \quad \lvert\hat{z}\rvert \le \beta_h \\ 1 - \frac{\lvert\lvert\hat{z}\rvert - \beta_h\rvert}{\alpha_h - \beta_h}, & \lvert\hat{x}\rvert \le \beta_w, \quad \lvert\hat{z}\rvert \ge \beta_h \\ 1 - \frac{\lvert\lvert\hat{x}\rvert - \beta_h\rvert}{\alpha_w - \beta_w}, & \lvert\hat{x}\rvert \ge \beta_w, \quad \lvert\hat{z}\rvert \le \beta_h \\ 1 - \frac{\lvert\lvert\hat{z}\rvert - \beta_h\rvert}{\alpha_h - \beta_h} - \frac{\lvert\lvert\hat{x}\rvert - \beta_h\rvert}{\alpha_w - \beta_w}, & \lvert\hat{x}\rvert \ge \beta_w, \quad \lvert\hat{z}\rvert \ge \beta_h \end{cases}$ where $h = \frac{1}{4\beta_w\beta_h + 2\beta_w(\alpha_h - \beta_h) + 2\beta_h(\alpha_w - \beta_w) + \frac{2}{3}(\alpha_w - \beta_w)(\alpha_h - \beta_h)}$	(5)
	Incremental cumulative shear strain	$d\xi(\hat{x},\hat{z}) = \xi_{ref}\mu(\hat{x},\hat{z})d\hat{\delta}$	(6)
	Excess pore pressure generation due to undrained shearing	$\frac{\delta u_e(\hat{x},\hat{z})}{\delta\xi(\hat{x},\hat{z})} = \frac{\chi}{\xi_{99}}\left[\frac{\sigma`_v(\hat{x},\hat{z}) - \sigma`_{v,RSL}(\hat{x},\hat{z})}{\sigma`_{v,NCL}(\hat{x},\hat{z}) - \sigma`_{v,RSL}(\hat{x},\hat{z})}\right]^p$	(7)
Maintained loading	Stress distribution factor	$\Delta u_e(\hat{x},\hat{z}) = \begin{cases} \left(\frac{1 - \text{sign}(v_p)}{2} - \eta\right)\left[\frac{6}{\pi}\iint_{\mathbb{R}} Q(\mathbb{R})\frac{(\hat{z}_c - \hat{z})^3}{[4\hat{x}^2 + (\hat{z} - \hat{z}_c)^2]^{\frac{5}{2}}}d\mathbb{R}\right], & \hat{z} < \hat{z}_c \\ \left(\frac{1 + \text{sign}(v_p)}{2} - \eta\right)\left[\frac{6}{\pi}\iint_{\mathbb{R}} Q(\mathbb{R})\frac{(\hat{z} - \hat{z}_c)^3}{[4\hat{x}^2 + (\hat{z} - \hat{z}_c)^2]^{\frac{5}{2}}}d\mathbb{R}\right], & \hat{z} \ge \hat{z}_c \end{cases}$	(8)
Consolidation	Excess pore pressure dissipation	$\frac{\delta u_e(\hat{x},\hat{z})}{\delta t} = -\frac{u_{e,i}(\hat{x},\hat{z},t)\cdot c_v{}^m \cdot t^{m-1}\cdot(D^2T_{50})^m \cdot m}{[(D^2T_{50})^m + (c_v t)^m]^2}$	(9)
	Changes in specific volume	$\Delta v(\hat{x},\hat{z}) = -\kappa \ln\left[\frac{\sigma'_{vc}(\hat{x},\hat{z})}{\sigma'_v(\hat{x},\hat{z})}\right] - \lambda \ln\left[\frac{\sigma'_v(\hat{x},\hat{z}) + \Delta\sigma'_v(\hat{x},\hat{z})}{\sigma'_{vc}(\hat{x},\hat{z})}\right]$	(10)
Strength response	Lumped strength parameter	$\Phi(\hat{x},\hat{z}) = \{[OCR(\hat{x},\hat{z})]^b - 1\}\Phi_{steady} - \{[OCR(\hat{x},\hat{z})]^b - 1\}\left[1 - e^{-3\xi(\hat{x},\hat{z})/\xi_{95,\Phi}}\right]\Phi_{steady}$	(11)
	Undrained shear strength	$s_u(\hat{x},\hat{z}) = \Phi\sigma`_v(\hat{x},\hat{z})$	(12)
	Averaged undrained shear strength	$s_{u,av} = \int_V s_u(\hat{x},\hat{z})\cdot\mu(\hat{x},\hat{z})dV$	(13)
	Mobilised undrained shear strength	$\delta\left(\frac{s_{u,mob}}{s_{u,av}}\right) = \delta(\hat{x},\hat{z})K$	(14)
		$K = \left\{\left[\frac{\Delta(s_{u,mob}/s_{u,av})}{\Delta(s_{u,max}/s_{u,av})}\right]^\zeta\right\}K_{max}$	(15)

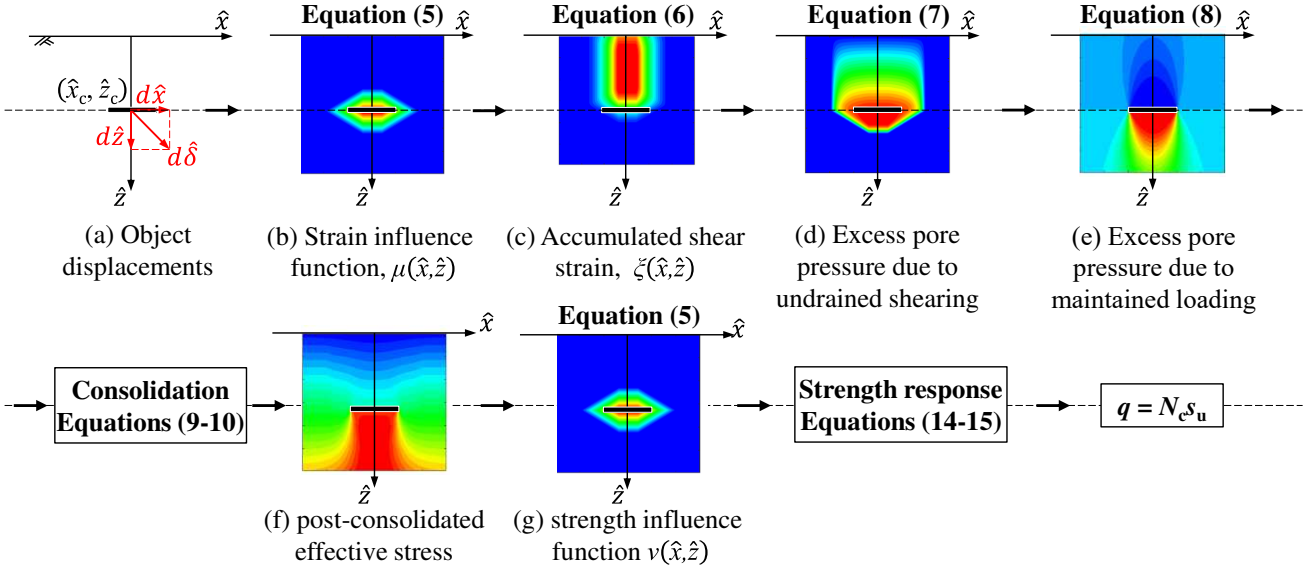

Figure 2. Schematic representation of analysis procedure

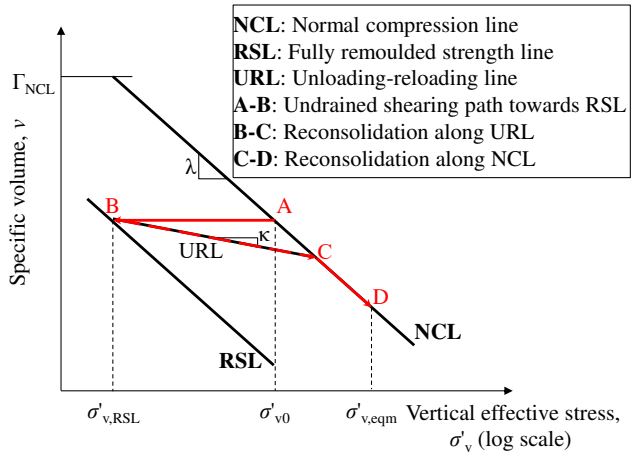

Figure 3. Illustration of the effective stress framework: changes in vertical effective stress and specific volume during undrained loading, reconsolidation and maintained load

An example LDFE analysis conducted using the 'remeshing and interpolation technique with small strain' (RITSS) technique for Abaqus (Tian et al. 2014) is provided in Figure 4 for the case of a deeply embedded horizontal circular plate with a smooth interface moving vertically through undrained clay (with and without strain softening). The complex distribution shown by Figure 4 can be simplified by employing the average concept, whereby ξ is integrated along the direction of interest (Einav & Randolph, 2005; Hodder et al., 2010). Profiles of accumulated plastic shear strain in the vertical direction, ξ_z, and in the horizontal direction, ξ_x, are provided in Figure 5, which also includes the 2D strain influence function, $\mu(\hat{x}, \hat{z})$ (Equation 5 in Table 1) defined by four shape parameters, α_w, α_h, β_w and β_h that satisfy $\int_{\hat{z}_c-\alpha_h}^{\hat{z}_c+\alpha_h}\int_{\hat{x}_c-\alpha_w}^{\hat{x}_c-\alpha_w} \mu(\hat{x},\hat{z})d\hat{x}d\hat{z} = 1$.

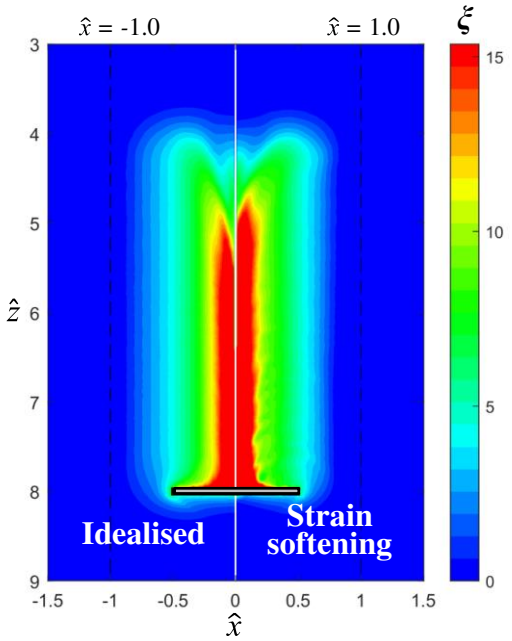

Figure 4. Contour plots of accumulated plastic shear strain, ξ (LHS: no softening; RHS: softening) for a deeply embedded horizontal circular plate undergoing vertical motion

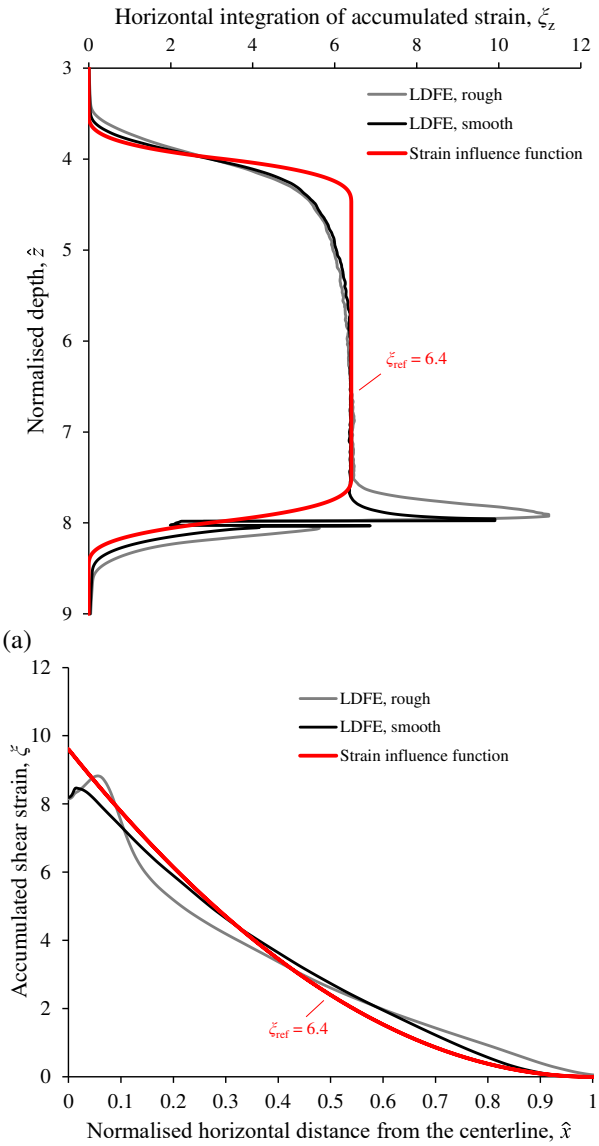

Figure 5. Comparison between LDFE simulations and strain influence zone idealisations for a circular plate: (a) vertical profiles; (b) horizontal profiles

2.3 *Excess pore pressure from maintained loads*

Excess pore pressure is induced by undrained shearing, but also by changes in total stress when the foundation is subjected to a maintained load. The additional excess pore pressure, $\Delta u_e(\hat{x}, \hat{z})$, in the 2D framework is calculated using elastic solutions that account for the total stress 'sharing' above and below the embedded object (Equation 8, see Table 1).

3 EXAMPLE SIMULATIONS

The merit of the 2D effective stress framework is explored in this section through a series of simulations of inclined circular plate in normally consolidated clay undergoing incremental displacements, $\left(d\hat{\Delta} = \sqrt{(d\hat{x})^2+(d\hat{z})^2}\right)$ within the $\hat{x}$-$\hat{z}$ (2D) space considered in

the framework, where $\hat{x}$ and $\hat{z}$ establish the 2D coordinate system and denote normalised distances (by the diameter of the foundation, D) in the horizontal and vertical directions, respectively (see Figure 6). The domain is discretised uniformly along $\hat{x}$ and $\hat{z}$, with the midpoint of each discretised element representing the average soil response within the finite elemental area.

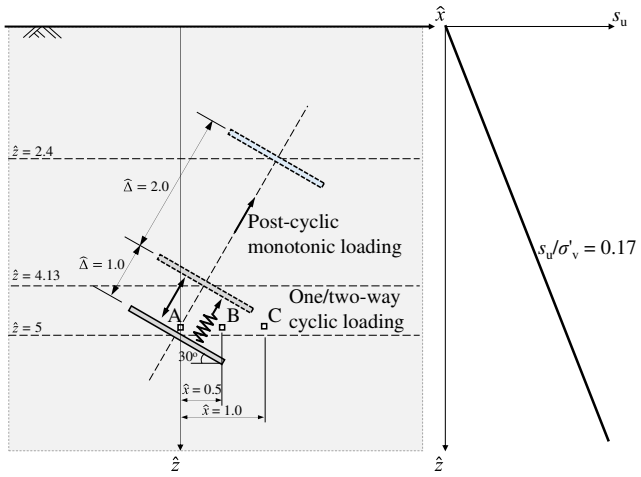

Figure 6. Problem definition for the example simulations

The following three calculation cases are considered:

1. Case 1 involves displacement-controlled monotonic loading for a displacement, $\hat{\Delta} = 2$ (where $\hat{\Delta}$ is the displacement of the plate, normalised by the plate diameter, D);
2. Case 2 involves 20 undrained displacement-controlled cyclic motions normal to the plate by $\hat{\Delta} = 1.0$, followed by displacement-controlled monotonic loading for a displacement, $\hat{\Delta} = 2$; and
3. Case 3 involves 10 packets of one-way load-controlled cyclic loading between q = 0 and $0.5q_0$ (where q_0 is the monotonic resistance at the initial embedment depth) with intervening consolidation periods under $q = 0.25q_0$ for a period that is sufficient for 90% consolidation between each packet, followed by displacement-controlled monotonic loading for a displacement, $\hat{\Delta} = 2$. This case is included to represent the type of loading (storms interspersed with periods of calm) that an offshore plate anchor in a taut or semi-taut mooring might experience over its lifetime.

The parameters adopted in the simulations are summarised in Table 2.

To demonstrate the different soil responses within the 2D domain, the three elements (A, B and C) shown on Figure 6 are considered. Figure 7 shows the effective stress paths followed by these three elements A, B and C for the three loading cases. The following observations are made:

(a) Undrained motion of the plate in case 1 softens the soil, generating excess pore pressure, u_e, that reduces the vertical effective stress, σ'_v, under constant volume conditions for all three elements. The reduction and hence minimum σ'_v is consistent with the amount of accumulated plastic shear strain developed at each element location. This will be highest at element A, which is just above the centreline of the plate and lowest for element C, which is located beyond the edge of the plate.

(b) Continued undrained cycling of the plate in case 2 causes further generation of excess pore pressure, reducing σ'_v for elements A, B and C to approach the limiting condition on the remoulded strength line (RSL). However, the rate of σ'_v degradation with cycle number reduces as the element becomes further from the centre of the plate (i.e., as $\hat{x}$ increases) as the accumulated plastic shear strain, ξ, reduces with increasing $\hat{x}$.

(c) The load-controlled cycles in case 3 lead to less excess pore pressure generation than in Cases 1 and 2. Indeed element C is not mobilised at all during cyclic loading due to the small accumulated displacements of the plate ($\Delta\hat{z} = 0.2$, see Figure 8), and only becomes mobilised in the post-cyclic monotonic loading stage. The 'zig-zag' effective stress paths for elements A and B represent the successive generation and dissipation of excess pore pressure in each packet of loading cycles, but with an increasing lower limit of σ'_v after each packet.

Table 2. Framework parameters

D	1 m	$\mathbf{T_{50}}$	0.05
γ'	7 kN/m^3	**m**	0.9
OCR	1	$\mathbf{\Phi_{steady}}$	0.6
$\mathbf{S_t}$	2.5	$\mathbf{\varepsilon_{95,\Phi}}$	28
Λ	0.205	**b**	0.65
K	0.044	$\mathbf{K_{max}}$	480
$\mathbf{(s_u/\sigma'_{vo})_{NC}}$	0.17	**ζ**	0.2
Λ	0.6	$\mathbf{\alpha_w}$	1.0
$\mathbf{\Gamma_{NCL}}$	3.251	$\mathbf{\alpha_h}$	0.5
$\mathbf{\varepsilon_{99}}$	100	$\mathbf{\beta_w}$	0
p	2.6	$\mathbf{\beta_h}$	0
η	0.1	$\mathbf{\xi_{ref}}$	6.4

Depth profiles of undrained shear strength due to the loading sequences for these three cases are shown on Figure 8. Case 1 follows the undrained shear strength line, whereas the average soil strength for case 2 is initially close to the remoulded strength line, but then emerges at the undrained strength profile at $\hat{z} = 3.27$. The volumetric hardening evident in Figure 7 for case 3 causes a 'breakthrough strength' that is 2.7 times the intact s_u at that depth ($\hat{z} = 4.61$), but then reduces with increasing displacement to also merge with an s_u line at $\hat{z} = 3.27$, but at a strength that is slightly higher than the undrained shear strength due to the excess pore pressure generated by the maintained resistance on the plate ($0.25q_0$).

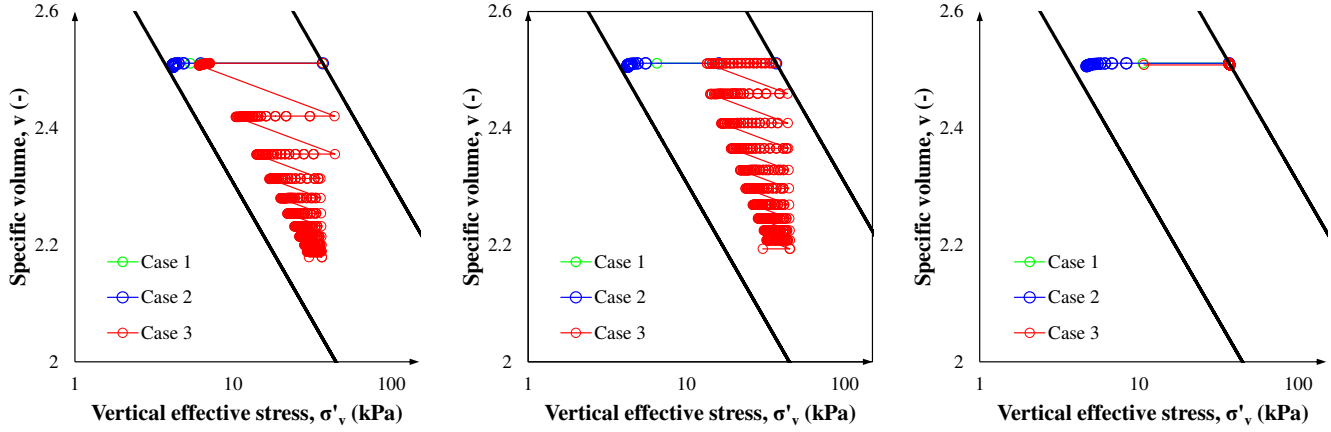

Figure 7. Effective stress paths from the simulations: element A (left), element B (middle) and element C (right)

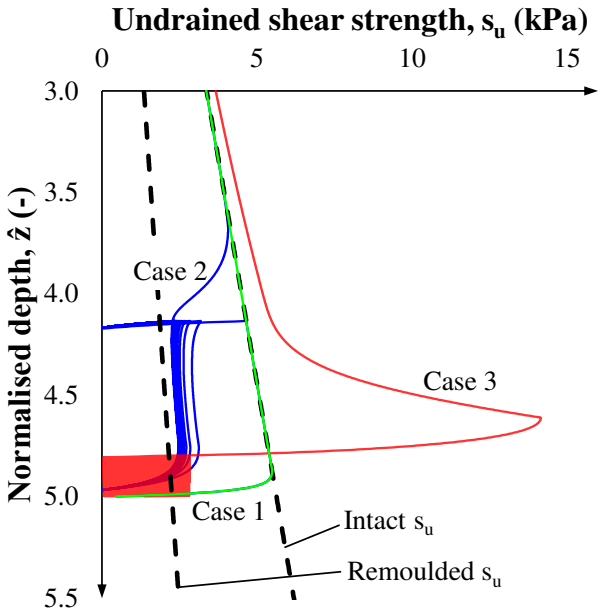

Figure 8. Simulated strength profiles

4 CONCLUSIONS

This paper considers an effective stress approach for calculating such spatial and temporal changes in soil strength around an embedded foundation. The work described here extends the existing framework developed by Zhou et al. (2019) but implemented within a 2D computational domain to allow for more credible consideration of problems that cannot be satisfactorily simplified to 1D conditions.

The framework can be readily coded and involves a small fraction of the computational time needed for effective stress based finite element simulations involving large deformations, making it suitable for use in design. Example simulations of an inclined circular plate in normally consolidated clay and subjected to loading normal to the plate demonstrate the potential of the framework. Other ongoing work considers the more complex (and realistic) case of a suction embedded plate anchor, for which the capacity mobilisation includes normal, shear and rotational load components. These and other applications of the framework for different boundary value problems will provide further confidence on the potential of this framework.

5 REFERENCES

Andersen, K.H., Lunne, T., Kvalstad, T.J., Forsberg, C.F. 2008. Deep water geotechnical engineering. *In Proc. 24th Nat. Conf. of Mexican Soc. of Soil Mechanics*, 1-57, Aguascalientes, Mexico.

Chow, S.H., O'Loughlin, C.D., Zhou, Z. 2020. Penetrometer testing in a calcareous silt to explore changes in soil strength. *Géotechnique*, **70(12)**, 1160-1173.

Cocjin, M.L., Gourvenec, S.M., White, D.J., Randolph, M.F. 2017. Theoretical framework for predicting the response of tolerably mobile subsea installations. *Géotechnique*, **67(7)**, 608-620.

Einav, I., Randolph, M. F. 2005. Combining upper bound and strain path methods for evaluating penetration resistance. *Int. J. Num. Methods Eng.*, **63(14)**, 1991-2016.

Feng, X., Gourvenec, S. 2015. Consolidated undrained load-carrying capacity of subsea mudmats under combined loading in six degrees of freedom. *Géotechnique*, **65(7)**, 563-575.

Gourvenec, S.M., Vulpe, C., & Murthy, T.G. 2014. A method for predicting the consolidated undrained bearing capacity of shallow foundations. *Géotechnique*, **64(3)**, 215-225.

Hodder, M.S., White, D.J., Cassidy, M.J. 2010. Analysis of soil strength degradation during episodes of cyclic loading, illustrated by the T-bar penetration test. *Int. J. Geomech.,* **10(3)**, 117-123.

Krabbenhøft, K., Galindo-Torres, S.A., Zhang, X., Krabbenhøft, J. 2019. AUS: Anisotropic undrained shear strength model for clays. *Int J. Numer. Anal. Methods Geomech.*, **43**, 2652–2666.

Randolph, M.F. 2013. 2nd McClelland Lecture: Analytical Contributions to Offshore Geotechnical Engineering. *Proc. 18th Int. Conf. on Soil Mech. & Geotech. Eng.*, Paris, 85-105.

Tian, Y, Cassidy, M.J., Randolph, M.F., Wang, D. & Gaudin, C. (2014). A simple implementation of RITSS and its application in large deformation analysis. Comput. Geotech., **56**, 160-167.

Zhou, Z., White, D.J., O'Loughlin, C.D. 2019. An effective stress framework for estimating penetration resistance accounting for changes in soil strength from maintained load, remoulding and reconsolidation. *Géotechnique*, **69(1)**, 57-71.